Modeling Nongray Gas-Phase and Soot Radiation in Luminous Turbulent Nonpremixed Jet Flames

L. Wang, M. F. Modest, D. C. Haworth† and S. R. Turns

Department of Mechanical & Nuclear Engineering
The Pennsylvania State University
University Park, PA 16802
USA

PACS numbers: 44.40.+a Thermal radiation; 47.27.-i Turbulent flows, convection, and heat transfer; 47.70.-n Reactive, radiative, or nonequilibrium flows.

Abstract. Much progress has been made in radiative heat transfer modeling with respect to treatment of nongray radiation from both gas-phase species and soot particles, while radiation modeling in turbulent flame simulations is still in its infancy. Aiming at reducing this gap, this paper introduces state-of-the-art models of gas-phase and soot radiation to turbulent flame simulations. The full-spectrum k-distribution method (M.F. Modest, Journal of Quantitative Spectroscopy & Radiative Transfer 2003, 76: 69-83) is implemented into a three-dimensional unstructured CFD code for nongray radiation modeling. The mixture full-spectrum k-distributions including nongray absorbing soot particles are constructed from a narrow-band k-distribution database created for individual gas-phase species, and an efficient scheme is employed for their construction in CFD simulations. A detailed reaction mechanism including NO_x and soot kinetics is used to predict flame structure, and a detailed soot model using a method of moments is employed to determine soot particle size distributions. A spherical-harmonic P_1 approximation is invoked to solve the radiative transfer equation. An oxygen-enriched, turbulent, nonpremixed jet flame is simulated, which features large concentrations of gas-phase radiating species and soot particles. Nongray soot modeling is shown to be of greater importance than nongray gas modeling in sooty flame simulations, with gray soot models producing large errors. The nongray treatment of soot strongly influences flame temperatures in the upstream and the flame-tip region and is essential for accurate predictions of NO. The nongray treatment of gases, however, weakly influences upstream flame temperatures and, therefore, has only a small effect on NO predictions. The effect of nongray soot radiation on flame temperature is also substantial in downstream regions where the soot concentration is small. Limitations of the P_1 approximation are discussed for the jet flame configuration; the P_1 approximation yields large errors in the spatial distribution of the computed radiative heat flux for highly anisotropic radiation fields such as those in flames with localized, near-opaque soot regions.

Revised version, submitted to: *Combust. Theory Modelling* 25 March 2005

† To whom correspondence should be addressed (dch12@psu.edu)

1. Introduction

Thermal radiation plays an important role in combustion and flames. Inadequate treatment of radiation can cause large errors in determining the flame structure and pollutant emissions. For example, the prediction of NO_x emissions is very sensitive to the prediction of the flame temperature distribution [1]. Similarly, soot formation/oxidation and radiation are highly coupled processes. Errors in temperature predictions result in over- or under-predicted soot formation and oxidation rates and, therefore, soot yields, which in turn result in erroneous radiative heat loss values. Consequently, a detailed description of radiative energy transfer is an essential element in turbulent combustion simulations.

Radiative heat transfer in turbulent flames enters the overall energy conservation equation through a heat source term, which is expressed as the divergence of the radiative heat flux, $\vec{q}_R$,

$$\nabla \cdot \vec{q}_R = \int_0^\infty \kappa_\eta \left(4\pi I_{b\eta} - \int_{4\pi} I_\eta \mathrm{d}\Omega \right) \mathrm{d}\eta = \int_0^\infty \kappa_\eta \left(4\pi I_{b\eta} - G_\eta \right) \mathrm{d}\eta. \qquad (1)$$

Here η is wavenumber, Ω is solid angle, κ_η is the spectral absorption coefficient, I_η is the spectral radiative intensity, and $G_\eta = \int_{4\pi} I_\eta \mathrm{d}\Omega$ is the direction-integrated spectral incident radiation; subscript b denotes a blackbody property [2]. The absorption coefficient may contain contributions from both gas-phase species and particulates. The radiative intensity is determined from the solution of the radiative transfer equation (RTE) [2]:

$$\frac{\mathrm{d}I_\eta}{\mathrm{d}s} = \hat{s} \cdot \nabla I_\eta = \kappa_\eta I_{b\eta} - \beta_\eta I_\eta + \frac{\sigma_{s\eta}}{4\pi} \int_{4\pi} I_\eta(\hat{s}_i) \Phi_\eta(\hat{s}_i, \hat{s}) \mathrm{d}\Omega_i, \qquad (2)$$

where β_η is the spectral extinction coefficient; this is the sum of the spectral absorption coefficient κ_η and the spectral scattering coefficient $\sigma_{s\eta}$. The quantity $\Phi_\eta(\hat{s}_i, \hat{s})$ is the scattering phase function and describes the probability that a ray from a specified direction, $\hat{s}_i$, is scattered into a specified other direction, $\hat{s}$.

Accurate evaluation of radiative heat transfer in turbulent flames is extremely difficult. Three challenges are: the solution of the RTE (a five-dimensional integro-differential equation), the spectral behavior of the radiating species and the spectral integration of Equations (1) and (2), and the evaluation of turbulence-radiation interactions. Turbulence-radiation interactions are beyond the scope of the present paper, and the reader is referred to the pertinent literature [3–10].

Because of the difficulties associated with radiation calculations, it has been the common practice in turbulent flame simulations to invoke the optically-thin approximation, and/or to assume the medium to be gray, for both luminous [11–13] and nonluminous [14] flames. The optically-thin radiation model can result in substantial error due to its neglect of self-absorption effects, as has been shown by both numerical and experimental studies [1, 15]. The gray medium assumption can also result in large errors as will be shown in the following. Nongray radiation modeling has begun to draw attention in combustion simulations [8, 16–18], and spectral radiation measurements have been conducted recently to provide experimental guidance [9, 19, 20].

Methods for the solution of the RTE in turbulent combustion simulations include the spherical harmonics P_1 method [7], the discrete ordinates (S_N) method [8], and the discrete

transfer method [21]. Among these methods, the P_1 method is the most straightforward to implement, yet it is powerful and has been found to be satisfactory in many combustion applications. Its applicability to highly sooting turbulent jet flames is discussed in this paper. Models for nongray radiative properties include the weighted sum of gray gases (WSGG) model [17], the spectral line-based weighted sum of gray gases (SLW) model [8], and the full spectrum k-distribution (FSK) method [16]. It has been shown that the FSK method is superior to the WSGG model and that the SLW model is essentially a crude implementation of the FSK method [22]. The FSK method has undergone several major developments since its introduction and has become one of the most promising models for radiative heat transfer in inhomogeneous nongray media [23]. One recent development of the FSK method has been the construction of mixture full-spectrum k-distributions from a narrow-band k-distribution database created for individual gas species [24]. This development makes it possible to account for nongray soot radiative properties.

Soot radiation constitutes an important part of the total flame radiation in luminous flames. The determination of soot radiation in a realistic radiation model involves determination of soot particle size distributions in flames, as well as modeling of radiative properties of individual soot particles. Because of the difficulties in soot modeling, soot quantities computed in flame simulations usually are limited to soot total number density and soot mass or volume fraction. Because of the complex structure of soot particles and the uncertainties in soot refraction index, soot radiation in turbulent flames has been treated commonly using the optically-thin approximation with the assumption of gray soot [25].

The purpose of this paper is to apply recent developments of the FSK method to turbulent flame simulations for nongray gas-phase and soot radiation modeling, and thereby to establish the relative importance of nongray gas and soot radiation properties. Three radiation models are implemented into a three-dimensional unstructured CFD code: one that accounts for nongray properties of both gas species and soot particles, one that considers nongray gases but gray soot, and one that assumes both gases and soot to be gray. The FSK method is employed for nongray radiation modeling, and Planck-mean absorption coefficients are used for gray medium properties. All the radiation models include self-absorption and employ the spherical harmonic P_1 method for the RTE solution. A detailed reaction mechanism containing 122 chemical species and 677 elementary reactions is employed to model gas-phase chemistry. A detailed soot model and a method of moments are employed to determine the soot particle size distribution function (PSDF), which is then used to calculate soot radiation. The effects of nongray soot and gas-phase radiation on flame radiant heat flux, temperature, and NO_x emissions are discussed for an oxygen-enriched, turbulent, nonpremixed jet flame.

The remainder of this paper is organized as follows. The modeled flame configuration is presented in the next section. This is followed by descriptions of the numerical and physical models employed in the simulation; these include the underlying CFD code, turbulence and combustion models, chemical kinetics, and soot calculations. Radiation modeling is developed in detail in a separate section; here the novel nongray soot treatment is a major focus. The effects of nongray gas-phase and soot radiation properties are discussed for an oxygen-enriched turbulent nonpremixed propane flame. And conclusions are summarized in

the final section.

2. Flame configuration

The modeled flame is a turbulent nonpremixed propane jet flame with fuel issuing from a 3-mm-i.d. nozzle at a velocity of 21.8 m/s (the jet Reynolds number is approximately 15,000) [26]. The oxygen-enriched laminar coflow of 200-mm i.d. contains 40% oxygen by volume. It has been found experimentally, and confirmed using a simple two-stage Lagrangian model [26], that 40% oxygen enrichment results in the largest soot concentrations, and those in turn make a large contribution to the total radiative heat loss. Oxygen-enriched flames feature higher flame temperature and higher concentrations of radiatively participating H_2O and CO_2 compared to conventional hydrocarbon-air flames, since the heat sink and diluent effects of nitrogen are diminished [27]. In addition, the increased temperature promotes soot formation. These characteristics make both nongray gas-phase and soot radiation important. Available measurements include global quantities such as NO_x emission index ($EINO_x$) [28] and radiant fraction (ratio of the total radiative heat loss to the chemical heat release), and axial profiles of radiant heat flux at the peripheral side of the flame [26]. The burner configuration is sketched in Figure 1.

3. Numerical and physical models

3.1. Turbulent flow field

The underlying CFD code [29] solves the Favre-averaged compressible flow equations using a finite-volume method on an unstructured mesh. The equations include conservation of mass, momentum, absolute enthalpy, and chemical species. Gradient-transport models are invoked for turbulent transport and a standard k-ε model is employed. An iteratively implicit, pressure-based, segregated solution procedure solves the coupled system of governing pde's for collocated cell-centered variables. Here the computational configuration is axisymmetric and steady-state solutions are reached by time marching.

3.2. Chemical kinetics and turbulence-chemistry interactions

Detailed chemical mechanisms are required to describe soot formation/oxidation and NO_x production. The mechanism used here integrates the mechanism taken from Appel et al. [30] for soot precursor (polycyclic aromatic hydrocarbon, PAH) growth and oxidation with mechanisms taken from GRI_Mech 3.0 [31] for NO_x formation and propane oxidation. The resulting mechanism contains 122 chemical species and 677 elementary reactions [32], and is implemented using CHEMKIN [33]. The same mechanism was used in an earlier two-stage Lagrangian modeling study for oxygen-enriched flames [26]. In the present CFD-based modeling study, *in situ* adaptive tabulation [34] has been used to accelerate the chemistry calculations.

Table 1. Turbulence (k-ε) and combustion model constants.

symbol	C_1	C_2	C_μ	σ_k	σ_ε	C_m
value	1.48	1.92	0.09	1.0	1.3	0.09

A variant of an eddy-breakup model, a characteristic-time-scale model [35], has been employed to account for the effects of turbulence on mean chemical reaction rates. In this model, the mean reaction rate of species i is determined by a kinetic timescale $\tau_{kin,i}$ and by a turbulence timescale τ_{turb},

$$\dot{\omega}_i = \frac{Y_i^* - Y_i}{\tau_{kin,i} + f\tau_{turb}}. \tag{3}$$

Here Y_i is the species-i mass fraction, Y_i^* is the corresponding equilibrium mass fraction, and $\tau_{kin,i}$ is a kinetic time scale. The turbulence time scale τ_{turb} is the eddy turnover time computed as $C_m k/\epsilon$, where k and ϵ are the turbulence kinetic energy and its dissipation rate, respectively, and C_m is a model coefficient; here C_m= 0.09, the same value as C_μ in a standard $k-\epsilon$ model. The quantity f is a reaction progress variable that ranges from zero to unity as combustion proceeds. The specifications of Y_i^*, $\tau_{kin,i}$, and f are discussed in [35]. This simple turbulent combustion model serves to reduce the mean rate of heat release where turbulent mixing becomes rate controlling. A transported probability density function method that more accurately captures the effects of turbulence-chemistry interactions with detailed chemical kinetics [36] will be used in future studies.

Table 1 summarizes the model constants employed in the turbulence and combustion models. These model constants have been selected such that the simulated flame zone (mean temperature contour) is consistent with the measured visible flame size.

3.3. Soot

The soot model includes detailed descriptions of the formation and oxidation of PAH's, the nucleation of the first soot particles, coagulation, surface growth and condensation, and oxidation of soot particles [30, 37]. The gas-phase chemistry for PAH's includes species up to four-ring aromatics (pyrene). The occurrence of the smallest soot particles results from the coagulation of two PAH's. These particles grow through surface reactions and condensation of PAH molecules. They can also be removed by oxidation as a result of surface reactions with molecular oxygen and OH radicals.

The evolution of the soot PSDF due to soot nucleation, coagulation, surface growth, and oxidation is described by the method of moments [38]. The rth soot moment of the PSDF, M_r, is defined as

$$M_r = \sum_{i=1}^{\infty} m_i^r N_i \quad \text{for } r = 0, 1, \ldots, \infty, \tag{4}$$

where m_i and N_i are the particle mass and number density of size class i, respectively. Then, the zeroth moment is the total number density of soot particles, the first moment is

the total mass density, and so on. In principle, knowledge of all the moments is equivalent to knowledge of the PSDF itself. In most practical applications, however, the properties of interest are fully determined by just the first few moments [38]: for example, soot volume fraction can be deduced from the first moment. This results in the numerical economy of the method of moments.

Transport equations for soot moments have been derived [25, 32] and the mean moment transport equations solved in the CFD code are written as:

$$\frac{\partial(\bar{\rho}\tilde{M}_{mr})}{\partial t}+\frac{\partial(\bar{\rho}\tilde{u}_i\tilde{M}_{mr})}{\partial x_i}=\frac{\partial}{\partial x_i}\left(\frac{\mu_T}{Pr_{T,s}}\frac{\partial\tilde{M}_{mr}}{\partial x_i}\right)+\overline{\left.\frac{\mathrm{d}M_r}{\mathrm{d}t}\right|_s}, \quad r=0,1,\ldots,5, \tag{5}$$

where the over-bar and tilde denote Reynolds- and Favre-averaged mean quantities, respectively. Here $M_{mr} = M_r/\rho$, where ρ is the density of the gas-phase mixture. Then $\bar{M}_r$ and $\tilde{M}_{mr}$ are related by $\bar{M}_r = \bar{\rho}\tilde{M}_{mr}$. The molecular diffusion term has been neglected and a gradient-transport model has been invoked for turbulent transport. The quantity μ_T is the effective turbulence viscosity determined by the k-ε turbulence model ($\mu_T = C_\mu\bar{\rho}k^2/\varepsilon$), and $Pr_{T,s}$ is an effective turbulent Schmidt number that is set to unity in our calculations. The mean source terms in Equation (5) are evaluated using the mean quantities calculated from the CFD code, i.e., neglecting the influence of turbulent fluctuations.

There are discrepancies between the predicted and measured soot distribution as reported in the study of Wang et al. [25]. To facilitate the present study of nongray effects, the soot distribution used for the radiation calculations is obtained as follows. Transport equations for soot moments are solved together with other conservation equations in the CFD code and the distribution of soot volume fraction (f_v, used in determining soot radiation) is obtained. This distribution of f_v(z,r) then is adjusted to match that obtained from experiments. Values of the correction factors in the high-soot region are less than a factor of two. Finally, this adjusted f_v distribution is imposed on the same computational grid with the soot moment calculations turned off.

4. Radiation models

4.1. The FSK method

The FSK model is an extension of the narrow-band k-distribution model [39] to the entire spectrum by introducing a fractional Planck function [22]. The essence of the k-distribution method is a reordering process. It is observed that, over a narrow spectral range, the rapidly oscillating absorption coefficient (e.g., the upper frame of Figure 2) attains the same value many times at different wavenumbers, each time resulting in identical radiative intensity if the RTE is solved for a homogeneous medium. Conducting such identical calculations repeatedly contributes to the expense of line-by-line calculations. If the detailed spectral information is ignored, and one considers instead the probability that the absorption coefficient takes a particular value across the spectrum, then the rapidly-changing absorption coefficient in spectral wavenumber space can be reordered in the so-called g space, where g is the cumulative distribution function of absorption coefficient over a spectral range. The resultant

k-distribution, the absorption coefficient variable $k\ vs.\ g$, is a well-behaved smooth function (e.g., the lower frame of Figure 2). The tedious integration over wavenumber space can then be replaced by integration over g space using a small number of quadrature points. This is the virtue of the k-distribution method.

To extend the narrow-band k-distribution method to the full spectrum, the variation of blackbody intensity across the whole spectrum has to be considered. By introducing a fractional Planck function, the FSK method is obtained using an approach that is similar to that used for the WSGG model; the latter can be shown to be a crude implementation of the FSK method [22]. Alternatively, the FSK method can be obtained directly by multiplying the RTE by a Dirac-delta function, followed by integration over the entire spectrum [40].

The FSK method provides an accurate and effective means for the spectral integration of radiative quantities that appear, for example, in Equations (1) and (2). For homogeneous media, it achieves the accuracy of line-by-line (LBL) calculations at a tiny fraction of LBL's computational cost. For inhomogeneous media, the assumption of correlated absorption coefficients is usually invoked; that leads to two versions of the FSK method, the full-spectrum correlated-k (FSCK) method and the full-spectrum scaled-k (FSSK) method [40]. The error introduced by the correlated absorption coefficients assumption can be further reduced by a multi-scale approach [23], but this approach is still under development. Here the FSSK method for inhomogeneous media has been employed since it generally outperforms the FSCK method [40].

Employing FSSK, the radiative heat source term (Eq. 1) becomes

$$\nabla \cdot \vec{q}_R = \int_0^1 ku(4\pi a I_b - G_g)\mathrm{d}g. \tag{6}$$

Here k is the reordered local mixture absorption coefficient (κ_η) evaluated at a reference state, and k is a function of the spectral g variable weighted by the Planck function. The quantities u and a are, respectively, a scaling function that incorporates the spatial variations of the absorption coefficient, and a nongray stretching factor accounting for varying local temperatures in the Planck function that is used to construct the k-g distributions [22, 40]. The reference state (temperature and radiating species mole fractions) and the u function are determined according to the formulae given by Modest [2]. Programs to construct k-g distributions and the a functions are available for download [2]. Finally, the term G_g is the spectral incident radiation in g-space. It is obtained by solving the FSK-reordered radiative transfer equation [22, 40].

4.2. The P_1 approximation

The FSK method is designed to work with any RTE solution method. Here the spherical harmonic P_1 Approximation is employed, since it is straightforward to implement yet powerful and accurate for many combustion systems. The spherical harmonic method transforms the RTE into a set of simultaneous partial differential equations by expressing the radiative intensity as a series of products of angular (directional) and spatial functions. The angular dependence is represented using spherical harmonics, and the spatial functions

then are solved for. The number of terms retained in the series expansion gives the method its order and its name: for example, the P_1 or the P_3 approximation. With P_1, the FSK-reordered RTE becomes [32]

$$\nabla \cdot \frac{1}{ku} \nabla G_g - 3ku\,(G_g - 4\pi a I_b) = 0, \tag{7}$$

with the boundary condition

$$-\frac{2(2-\epsilon)}{3\epsilon} \hat{n} \cdot \nabla G_g + kuG_g = 4\pi ku a_w I_{bw}. \tag{8}$$

Here $\hat{n}$ is the inward-pointing unit surface normal at a boundary, ϵ is the surface emittance, and a_w and I_{bw} are evaluated at the surface temperature T_w. For the flame configuration shown in Figure 1, the surface emittance is set to unity to mimic a black surface and the surface temperature is set according to experimental measurements. The incident radiation G_g is evaluated at representative "spectral" g locations, whose values are usually determined by a Gaussian quadrature scheme. Ten or fewer quadrature points generally suffice because of the smooth behavior of k in g-space (Figure 2). Here nine quadrature points have been used, thus requiring the solution to nine equations of the form of Equations (7) and (8).

4.3. Nongray soot treatment

The local mixture k-g distributions consist of contributions from gas-phase species and soot particles, and they are constructed from the sum of gas-phase and soot absorption coefficients. The gas-phase absorption coefficient, in turn, consists of contributions from each of its component gases (e.g., CO_2 and H_2O). During a CFD simulation of a flame, it is computationally intensive to calculate the local mixture k-distributions directly from mixture absorption coefficients (provided that gas-phase absorption coefficients have already been determined from a spectral line database): the local mixture k-distributions have to be determined for every computational cell/node at each time/iteration step, and radiation calculations constitute only a small part of a turbulent flame simulation. In practice, the k-distributions of each component gas species are precalculated and, during the flame simulation, the local gas mixture k-distributions are obtained by mixing the precalculated single-gas k-distributions (SGK's) according to the local gas mixture composition. The contribution from soot particles is then incorporated into the local gas mixture k-g distributions.

The SGK's can be constructed in two formats, viz., full-spectrum and narrow-band k-distributions. In the full-spectrum format, the mixing of component SGK's is performed at the full-spectrum level. This, however, excludes consideration of nongray soot particles: due to the nature of the FSK reordering process, mixing is accurate between gas species whose absorption coefficients vary "randomly" across the spectrum, but inaccurate between gases and soot particles, as the absorption coefficients for the latter vary smoothly and continuously across the spectrum (Rayleigh's theory has been applied; see below). In the full-spectrum format, soot must be treated as gray and its spectrally averaged mean property (a constant) can then be added directly to full-spectrum k-distributions of the gas mixture. In the narrow-band format, the mixing of component SGK's is performed at the narrow-band level and that

allows consideration of nongray soot particles: the absorption due to nongray soot can be added directly to the narrow-band k-distributions of the gas mixture, since the soot absorption coefficient is essentially constant across each narrow band [24]. Both formats of precalculated SGK's have been implemented in our calculations, leading to two different nongray radiation models: a fully nongray model with both gases and soot treated as nongray; and a semigray model where gases are treated as nongray while soot is assumed to be gray (with Planck-mean values for the latter).

The mixing model used to calculate gas-mixture k-distributions from SGK's is the one proposed by Riazzi and Modest [24]. This model is based on the uncorrelatedness between spectral lines of different gases, leading to multiplicative transmittance from which a rule of mixing SGK's was derived. This mixing model has been shown to result in virtually no error at the narrow-band level and small errors (less than 2%) at the full-spectrum level [24].

The nongray soot absorption coefficient is determined by applying Rayleigh's theory to an ensemble of polydisperse soot particles, which gives [2]

$$\kappa_\lambda = \frac{36\pi nk}{(n^2-k^2+2)^2+4n^2k^2}\frac{f_v}{\lambda}, \tag{9}$$

where λ is the wavelength in cm. The soot complex index of refraction, $m = n - ik$, is spectral in nature and is modeled using the correlations proposed by Chang and Charalampopoulos [41]:

$$n = 1.8110 + 0.1263\ln\lambda + 0.0270\ln^2\lambda + 0.0417\ln^3\lambda, \tag{10}$$

$$k = 0.5821 + 0.1213\ln\lambda + 0.2309\ln^2\lambda - 0.0100\ln^3\lambda. \tag{11}$$

Here λ is in μm and these correlations are valid over the wavelength range $0.4\mu\text{m} \leq \lambda \leq 30\mu\text{m}$. These correlations represent the state-of-the-art and have been confirmed by experimental studies [42].

4.4. Efficiency considerations

Mixing at the narrow-band level (to account for nongray soot) is demanding computationally. For example, the computation of the mixture k-distributions for a coarse CFD mesh of 5000 computational cells consumes about 35 seconds on a 2.8 GHz Intel Xeon processor for just one time/iteration step. Mixing at the full spectrum level, on the other hand, is much faster by almost a factor of the number of the narrow bands (about 250 for a sufficiently accurate narrow-band database [43]). Therefore, to achieve better efficiency, the computational domain is divided into two regions according to a threshold value of soot volume fraction: a soot-gas region and a gas-only region. For the gas-only region, both the fully nongray radiation model and the semigray model use precalculated full-spectrum SGK's to obtain the local mixture k-distributions. For the soot-gas region, the semigray model also uses full-spectrum SGK's for mixing (since soot is treated as gray), while the nongray model uses narrow-band SGK's to obtain local mixture k-distributions (since nongray soot is taken into account). The error introduced by mixing at the full-spectrum level was found to be less than 2% compared to mixing at the narrow-band level [24]. The threshold value of soot volume fraction is

determined such that the optical thickness of the computational domain for that value is less than 0.01 at the wavelength where the averaged blackbody intensity in the domain takes the maximum value.

If one neglects the weak dependence of spectral line broadening on species mole fractions, then the absorption coefficients are linearly dependent on species mole fractions. Using this approximation, mixture narrow-band k-distributions (MNBK's) can be precalculated for the soot-gas region and the expensive mixing process can then be avoided during a CFD simulation, as long as the mole fraction ratio of the component species in the mixture is fixed. This is the case for complete combustion of a hydrocarbon fuel, where the mole fraction ratio of radiatively participating species is fixed at the stoichiometric value (for example, the CO_2/H_2O ratio for propane flames is 0.75). In real flames, incomplete combustion and turbulent mixing can shift the ratios from their stoichiometric values. To deal with this, several MNBK's with different mole fraction ratios are precalculated, and interpolation/extrapolation is performed for mixtures of arbitrary species mole fraction ratios.

In our calculations, only CO_2 and H_2O are considered as radiatively participating; the contributions from CO and propane are ignored since their contributions are relatively small. It has been observed that the range of mole fraction ratios of CO_2 to H_2O for the soot-gas region (on the fuel-rich side of the flame) lies between the stoichiometric value (0.75) and 0.2. Therefore, MNBK's of four ratios (0.8, 0.6, 0.4, and 0.2) are databased. The H_2O mole fraction used for generating these MNBK's is the value in the stoichiometric combustion of propane with 40% O_2 and 60% N_2 (0.27). The full-spectrum SGK's and MNBK's in this work are precalculated from the high-accuracy narrow-band SGK database generated by Wang and Modest [43]. In Figure 3, the mixture full-spectrum k-distributions constructed from the precalculated full-spectrum SGK's and MNBK's (for the gas-only and soot-gas region, respectively) are compared with those constructed directly from the high-accuracy narrow-band SGK database. The mixture contains 5.5% CO_2 and 10% H_2O with a soot volume fraction of 7.5×10^{-07}. The figure shows that the differences are small and, therefore, the construction scheme of using precalculated full-spectrum SGK's and MNBK's is acceptable for CFD simulations. Differences between the mixture full-spectrum k-distributions with and without soot (soot-gas region and gas-only region in the figure) indicate the significant contribution of the soot to the mixture absorption coefficient.

4.5. Gray radiation model

To establish the importance of accounting for nongray radiation properties, a fully gray model also has been implemented. In this case, the radiative source term (Eq. 1) becomes [2],

$$\nabla \cdot \vec{q}_R = 4\pi\kappa_p I_b - \kappa_p G, \tag{12}$$

where κ_p is the Planck-mean absorption coefficient. To ensure a fair comparison, gas-phase Planck-mean absorption coefficients are determined from local gas-phase full-spectrum k-distributions, and soot Planck-mean absorption coefficients are determined from spectrally averaging Equation (9) at local conditions. The incident radiation G is determined by solving

Table 2. Summary of radiation models.

Radiation Model	Description	Gas-Only Region	Soot-Gas Region
Nongray	Nongray gas and nongray soot	Mixing of SGK's	Use of MNBK's
Semigray	Nongray gas and gray soot	Mixing of SGK's	Mixing of SGK's
Gray	Gray gas and gray soot	Planck-mean	Planck-mean

the RTE with the spherical harmonic P_1 method [2],

$$\nabla \cdot \frac{1}{\kappa_p} \nabla G - 3\kappa_p \left(G - 4\pi I_b\right) = 0, \tag{13}$$

subject to the boundary condition

$$-\frac{2}{3}\hat{n} \cdot \nabla G + \kappa_p G = 4\pi\kappa_p I_b. \tag{14}$$

Here unity surface emittance has been assumed.

4.6. Summary

Three radiation models, i.e., nongray, semigray, and gray models, have been described in this section. The three models are summarized in Table 2.

5. Results and discussion

5.1. Radiative heat source

Figure 4 shows contour plots of the divergence of the radiative heat flux (the radiation source term in the energy equation) predicted by the three radiation models for the oxygen-enriched propane flame. The contours correspond to a slice of the axisymmetric computational mesh, and the radial coordinate has been stretched for clarity. Isocontours of the soot volume fraction also are plotted. Since the radiative heat source is strongly dependent on flame temperature, its isocontours essentially indicate the location of the flame zone, where chemical reactions are most active. This figure shows that, overall, the gray model (gray soot and gray gases) predicts larger heat losses than the semigray model (gray soot and nongray gases), which in turn predicts larger heat losses than the fully nongray model (nongray soot and nongray gases). In gray models, the Planck-mean absorption coefficient is designed to predict the correct overall emission and fails to account properly for self-absorption; the latter is always underpredicted [2]. The difference in heat source prediction is more substantial between the nongray and the semigray model than between the semigray and the gray model, as can be seen by comparing the three contours in the flame-tip region (z between 0.35 and 0.6 m) and in the upstream flame zone (z less than 0.2 m). This suggests that the nongray soot treatment is more important than the nongray gases treatment in this sooty flame. The maximum value of soot volume fraction f_v is approximately 1.7×10^{-06}.

5.2. Flame temperature

Figure 5 shows contour plots of the mean flame temperatures predicted by the three radiation models. The temperature contours are generally consistent with the heat source contours. For example, in the flame-tip region the nongray model predicts higher temperatures than the semigray model, which in turn predicts higher temperatures than the gray model. The temperature contours also show that the difference in temperature prediction between the nongray and the semigray model is larger than between the semigray and the gray model. It is interesting to note that the flame zone (as indicated by high temperature) predicted by the nongray model, in addition to being broader in the flame-tip region, extends further downstream than does the flame zone predicted by the semigray and gray models. This suggests that the nongray radiation treatment, with its smaller heat loss, results in a longer flame than the gray radiation treatment.

The comparison of heat source and temperature contours gives a visual impression of the differences between the gray and nongray radiation models. To quantify these differences, axial and radial profiles of temperature and species mass fractions are examined. Figure 6 shows the axial profiles of centerline flame temperatures predicted by the three radiation models. It can be seen that the gray treatment of the radiatively participating medium overpredicts radiative heat loss and, therefore, underpredicts flame temperature. The difference in maximum axial flame temperature due to gray/nongray treatment of gases (the gray and semigray model), due to gray/nongray treatment of soot (the semigray and nongray model), and due to gray/nongray treatment of both gases and soot (the gray and nongray model) is approximately 149 K, 221 K, and 370 K, respectively. The difference in temperature due to gray/nongray soot is approximately 1.5 times larger than the difference due to gray/nongray gases. This demonstrates the importance of nongray soot radiation modeling in sooty flame simulations. In addition, the nongrayness of the soot and gases causes the flame zone to lengthen by about 5%, with the maximum temperature occurring approximately 0.03 m further downstream.

Figure 7 shows radial profiles of flame temperatures predicted by the three radiation models at three axial locations: one upstream, one in the flame-tip region, and one downstream. The differences between the semigray and the gray model (effects of nongray/gray gas modeling) again are relatively small compared to the differences between the nongray and the semigray model (effects of nongray/gray soot modeling). The nongray treatment of gases and soot leads to higher flame temperature throughout the computational domain. Nongray soot modeling shows a maximum effect near the flame-tip region, as seen in the profile at $z = 0.5$ m. This is consistent with the distribution of soot volume fraction shown in Figure 4. In the downstream region where there is little soot, the nongray soot model also has a large effect on the flame temperature distribution, as shown by the profile at $z = 0.8$ m, because hotter upstream gases are convected downstream. Table 3 tabulates the temperature differences between different radiation models at the three axial locations. In this table, the quantity ΔT_1 is the maximum temperature difference between predictions by the semigray and the gray model, ΔT_2 between the semigray and the nongray model,

Table 3. Maximum flame temperature differences due to different radiation models.

Axial Location	ΔT_1	ΔT_2	ΔT_3
$z = 0.2$ m	≈ 0	132	132
$z = 0.5$ m	146	262	408
$z = 0.8$ m	142	165	307

and ΔT_3 between the gray and the nongray model. In the upstream region, the temperature differences due to gray/nongray gas radiation model are essentially negligible. In the flame-tip region, the maximum temperature difference between nongray and gray soot models is approximately 1.8 times larger than that between nongray and gray gases models, while in the downstream region, the factor is approximately 1.2. This stronger effect on flame temperature in the upstream and flame-tip region has an impact on NO prediction, which is formed largely in those regions, as shown in the following.

5.3. NO_x prediction

Figure 8 shows radial profiles of calculated NO mean mass fractions resulting from the three radiation models at two axial locations. For clarity, the profiles at $z = 0.8$ m are not shown since they follow the same trends as the profiles at $z = 0.5$ m. The profiles at $z = 0.2$ m show that a large portion of the NO is generated in the upstream flame zone, and that the NO formation is extremely sensitive to flame temperature (see Figure 7 for temperature differences), and, therefore, to the radiation model. The profiles at $z = 0.5$ m also indicate that the differences in NO mass fraction due to nongray gases modeling are much smaller than the differences due to nongray soot modeling. The nongrayness of soot was shown in Figure 7 to have the strongest impact on flame temperature, especially in the upstream flame zone and the flame-tip region; therefore, nongray soot modeling is shown to be an essential element for accurate prediction of NO_x emissions in sooty flames.

The importance of nongray soot modeling can be further appreciated in Table 4, where the predicted NO_x emission indices and the radiant fractions from the three radiation models are compared with measured values. Both NO_x emission index and radiant fraction are indications of the overall flame temperature level, and the comparison between model predictions and measurements determines the overall performance of a radiation model. Table 4 shows that the gray and the semigray model overpredict the radiant fraction and, therefore, underpredict NO_x emissions; the nongray radiation model provides predictions that are the closest to the experimental values. The nongray model's overprediction of radiative loss likely comes from the simple turbulent combustion model, which leads to fast combustion and, therefore, overpredicted upstream flame temperatures [32]. The table also shows that the differences in radiant fraction among the three models are the same (0.08), while the difference in the NO_x emission index between the gray and the semigray model is much smaller than that between the nongray and the semigray model (0.9 vs. 14.0). This can be explained by the fact that a large portion of the NO is formed in the upstream flame zone, and

Table 4. Comparison of computed global quantities with experimental values.

Model	NO_x Emission Index	Radiant Fraction
Gray Model	10.2	0.51
Semi-Gray Model	11.1	0.43
Nongray Model	25.1	0.35
Experiment [26]	29.8	0.31

by the differences in upstream wall heat fluxes among the three models as shown in Figure 9.

5.4. Accuracy of the P_1 approximation

Figure 9 shows axial profiles of radiant heat fluxes (at $r = 0.1$ m, Figure 4) predicted by the three radiation models. The curve with symbols is obtained from the experiment [26]. The gray model greatly overpredicts the heat fluxes, as expected. The semigray model provides a peak value that is close to the experiment, but overall it also overpredicts the heat fluxes. Although the peak heat flux is underpredicted by the nongray model, the latter gives the best agreement in terms of the location of the peak and the overall radiation heat loss (proportional to the area under the profile). All the models show a flatter, less peaked distribution than the experiment. This has been traced to the the use of the P_1 approximation, as shown in the following analysis.

To identify the errors introduced by the P_1 approximation, two calculations are conducted. First, the CFD code is set up such that a small cylindrical hot zone of high constant temperature (2200 K) and large constant Planck-mean absorption coefficient (5000 1/m) exists in the middle of the cylindrical computational mesh to simulate the near-opaque soot region (Figure 4); the temperature and the Planck-mean absorption coefficient for the rest of the computational mesh are set to 300 K and a small constant value κ_{rest}, respectively; and the boundary is black and cold at 300 K. The radiant heat flux at the wall ($r = 0.1$ m) is then calculated using the P_1-gray model in the code. Second, the exterior of the small hot cylinder and the interior of the large cold cylinder ($r = 0.1$ m) are taken as black surfaces, and the radiant heat flux at $r = 0.1$ m is determined using view factors between the two black surfaces. Differences between the two calculations in the limit $\kappa_{rest} \to 0$ indicate inaccuracies in the P_1 method.

Figure 10 shows axial profiles of the radiant heat flux at $r = 0.1$ m from the two calculations. The numerical values attached to the P_1-gray curves (0.1, 0.3, and 1.0) are three different values of κ_{rest}. As the value of κ_{rest} decreases, or as the ratio of the absorption coefficient of the hot zone to the rest of the domain increases, the performance of the P_1 approximation becomes progressively worse. Mathematically, when the absorption coefficient ratio is very large, the P_1 governing Equation (Equations 7 and 13) for regions of small absorption coefficient reduces to a Laplace equation. Physically, since the P_1 method approximates the radiation intensity in a radiatively participating medium using the first-order spherical harmonic, P_1 is most appropriate for configurations where radiation comes from

all directions (approximately isotropic radiation). This analysis shows that the P_1 method is, in general, not suitable for quantitative radiation modeling in flames with near-opaque, localized soot regions because of the very anisotropic radiative intensity fields. However, the qualititative trends and conclusions that have been drawn earlier regarding nongray gas and soot radiation properties remain valid, as evidenced by the global quantity comparisons in Table 4 and the nongray model's good agreement with experiment in the overall radiative heat loss in Figure 9.

6. Conclusions

In this paper, the use of a narrow-band-based FSK method for nongray gas-phase and soot radiation modeling in the CFD simulation of luminous turbulent flames has been described, and the importance of nongray radiation modeling in predictions of radiant heat loss, flame temperature, and NO_x emissions has been discussed. An efficient scheme for constructing local full-spectrum k-distributions from precalculated full-spectrum single-gas k-distributions and mixture narrow-band k-distributions has been implemented for CFD simulations. The following conclusions can be drawn from the simulations of an oxygen-enriched turbulent nonpremixed jet flame:

- Gray models always overpredict radiative heat loss and underpredict flame temperature and NO_x emissions.
- Nongray soot modeling is of greater importance than nongray gas modeling in sooty flame simulations, with gray soot models producing large errors.
- The nongray treatment of soot strongly influences flame temperatures in the upstream and the flame-tip region and is essential for accurate predictions of NO formation in sooty flames.
- The nongray treatment of gases, however, weakly influences upstream flame temperatures and, therefore, has only a small effect on NO_x predictions.
- The nongrayness of soot also has a large effect on flame temperatures in downstream regions where the soot concentration is small.
- The spherical harmonic P_1 approximation to the RTE yields large errors in the spatial distribution of the computed radiative heat flux in flames with localized, near-opaque soot regions.

Acknowledgments

This research has been sponsored by National Science Foundation under Grant Number CTS-0121573, and by the GM R&D Center.

References

[1] J. H. Frank, R. S. Barlow, C. Lundquist, Radiation and nitric oxide formation in turbulent non-premixed jet flames, Proc. Combust. Institute 28 (2000) 447–454.

[2] M. F. Modest, Radiative Heat Transfer, 2nd Edition, Academic Press, New York, 2003.
[3] T. H. Song, R. Viskanta, Interactions of radiation with turbulence: Application to a combustion system, J. Thermophys. Heat Trans. 1 (1) (1987) 56–62.
[4] J. P. Gore, I. U. S., Y. R. Sivathanu, Coupled structure and radiation analysis of acetylene/air flames, ASME J. Heat Trans. 114 (1992) 487–493.
[5] J. W. Hartick, M. T. Tacke, G. Fruchtel, E. P. Hassel, J. Janicka, Interactions of turbulence and radiation in confined diffusion flames, Proc. Combust. Institute 26 (1996) 75–82.
[6] S. Mazumder, M. F. Modest, A PDF approach to modeling turbulence-radiation interactions in nonluminous flames, Intern'l. J. Heat Mass Trans. 42 (1998) 971–991.
[7] G. Li, M. F. Modest, Application of composition PDF methods in the investigation of turbulence-radiation interactions, J. Quant. Spectr. and Radiat. Trans. 73 (2002) 461–472.
[8] P. J. Coelho, O. J. Teerling, D. Roekaerts, Spectral radiative effects and turbulence/radiation interaction in a nonluminous turbulent jet diffusion flame, Combust. Flame 133 (2003) 75–91.
[9] Y. Zheng, Y. R. Sivathanu, J. P. Gore, Measurements and stochastic time and space series simulations of spectral radiation in a turbulent non-premxied flame, Proc. Combust. Institute 29 (2003) 1957–1963.
[10] Y. Wu, D. C. Haworth, M. F. Modest, B. Cuenot, Direct numerical simulation of turbulence/radiation interaction in premixed combustion systems, Proc. Combust. Institute 30 (2004) 639–646.
[11] M. J. Zimberg, S. H. Frankel, J. P. Gore, Y. R. Sivathanu, A study of coupled turbulent mixing, soot chemistry, and radiation effects using the linear eddy model, Combust. Flame 113 (1998) 454–469.
[12] X. S. Bai, M. Balthasar, F. Mauss, L. Fuchs, Detailed soot modeling in turbulent jet diffusion flames, Proc. Combust. Institute 17 (1998) 1623–1630.
[13] H. Pitsch, E. Riesmeier, N. Peters, Unsteady flamelet modeling of soot formation in turbulent diffusion flames, Combust. Sci. Technol. 158 (2000) 389–406.
[14] R. S. Barlow, website, http://www.ca.sandia.gov/TNF/, accessed on January 1, 2004.
[15] X. L. Zhu, J. P. Gore, A. N. Karpetis, R. S. Barlow, The effect of self-absorption of radiation on an opposed flow partially premixed flame, Combust. Flame 129 (2002) 342–345.
[16] S. Mazumder, M. F. Modest, Application of the full-spectrum correlated-k distribution approach to modeling nongray radiation in combustion gases, Combust. Flame 129 (2002) 416–438.
[17] O. J. Kim, J. P. Gore, R. Viskanta, X. L. Zhu, Prediction of self-absorption in opposed flow diffusion and partially premixed flames using a weighted sum of gray gases model (WSGGM)-based spectral model, Numerical Heat Transfer Part A-Applications 44 (4) (2003) 335–353.
[18] Y. Ju, G. Masuya, P. D. Ronney, Effect of radiative emission and absorption on the propagation and extinction of premixed gas flames, Proc. Combust. Institute 27 (1998) 2619–2626.
[19] J. Ji, Y. R. Sivathanu, J. P. Gore, Thermal radiation properties of turbulent lean premixed methane air flames, Proc. Combust. Institute 28 (2000) 391–398.
[20] Y. Zheng, R. S. Barlow, J. P. Gore, Measurements and calculations of spectral radiation intensities for turbulent non-premixed and partially premixed flames, Trans. of the ASME 125 (2003) 678–686.
[21] R. P. Cleaver, P. S. Cumber, M. Fairweather, Predictions of free jet fires from high pressure sonic releases, Combust. Flame 132 (2003) 463–474.
[22] M. F. Modest, H. Zhang, The full-spectrum correlated-k distribution for thermal radiation from molecular gas-particulate mixtures, Trans. ASME 124 (2002) 30–38.
[23] L. Wang, M. F. Modest, Narrow-band based multi-scale full-spectrum k-distribution method for radiative transfer in inhomogeneous gas mixtures, ASME J. Heat Trans., (2004) submitted.
[24] R. Riazzi, M. Modest, Assembly of full-spectrum k-distribution from a narrow-band database; effects of mixing gases, gases and nongray absorbing particles, and mixture with nongray scatters in nongray enclosures, J. Quant. Spectrosc. Radiat. Trans. in print.
[25] L. Wang, D. C. Haworth, S. R. Turns, M. F. Modest, Interactions among soot, thermal radiation, and NO_x emissions in oxgyen-enriched turbulent nonpremixed flames: A CFD modeling study, Combust. Flame (2005) to appear.
[26] L. Wang, N. E. Endrud, S. R. Turns, M. D. D'Agostini, A. G. Slavejkov, A study of the influence of oxygen index on soot, radiation, and emission characteristics of turbulent jet flames, Combust. Sci. Technol.

174 (8) (2002) 45–72.

[27] C. E. Baukal, Oxygen-Enhanced Combustion, CRC Press, Boca Raton, 1998.

[28] S. R. Turns, An Introduction to Combustion: Concepts and Applications, 2nd Edition, McGraw-Hill, New York, 2000.

[29] Y. Z. Zhang, D. C. Haworth, A general mass consistency algorithm for hybrid particle/finite-volume PDF methods, J. Comput. Phys. 194 (1) (2004) 156–193.

[30] J. Appel, H. Bockhorn, M. Frenklach, Kinetic modeling of soot formation with detailed chemistry and physics: Laminar premixed flames of C_2 hydorcarbons, Combust. Flame 121 (2000) 122–136.

[31] G. P. Smith, D. M. Golden, F. M., N. W. Moriarty, B. Eiteneer, M. Goldenberg, C. T. Bowman, R. K. Hanson, S. Song, W. C. Gardiner Jr., V. V. Lissianski, Z. Qin, website, http://www.me.berkeley.edu/gri_mech/, accessed on January 1, 2004.

[32] L. Wang, Detailed chemistry, soot, and radiation calculations in turbulent reacting flows, Ph.D. thesis, The Pennsylvania State University (2004).

[33] R. J. Kee, F. M. Rupley, J. A. Miller, Chemkin-II: A Fortran chemical kinetics package for the analysis of gas-phase chemical kinetics, Tech. Rep. SAND89-8009, Sandia National Laboratories (1989).

[34] S. B. Pope, Computationally efficient implementation of combustion chemistry using in situ adaptive tabulation, Combust. Theory & Modelling 1 (1) (1997) 41–63.

[35] S.-C. Kong, R. D. Reitz, Numerical study of HCCI engine combustion and its sensitivity to computational mesh and model uncertainties, Combust. Theory Modelling 7 (2) (2003) 417–433.

[36] Y. Z. Zhang, E. H. Kung, D. C. Haworth, A PDF method for multidimensional modeling of HCCI engine combustion: Effects of turbulence/chemistry interactions on ignition timing and emissions, Proc. Combust. Institute 30 (2004) 2763–2771.

[37] H. Wang, M. Frenklach, A detailed kinetic modeling study of aromatics formation in laminar premixed acetylene and ethylene flames, Combust. Flame 110 (1997) 173–221.

[38] M. Frenklach, Method of moments with interpolative closure, Chem. Engineering Sci. 57 (2002) 2229–2239.

[39] A. Lacis, V. Oinas, A description of the correlated k distribution method for modeling nongray gaseous absorption, thermal emission, and multiple scattering in vertically inhomogeneous atmosphere, J. Geophysical Research 96 (D5) (1991) 9027–9063.

[40] M. F. Modest, Narrow-band and full spectrum k distribution for radiative heat transfer - correlated-k vs. scaling approximation, J. Quant. Spectrosc. Radiat. Trans. 76 (2003) 69–83.

[41] H. Chang, T. T. Charalampopoulos, Determination of the wavelength dependence of refractive indices of flame soot, Proc. of the Royal Society (London), Ser. A 430 (1990) 577–591.

[42] Ü. Köylü, G. Faeth, Spectral extinction coefficients of soot aggregates from turbulent diffusion flames, ASME J. Heat Trans. 118 (1996) 415–421.

[43] A. Wang, M. F. Modest, High-accuracy, compact database of narrow-band k-distribution for water vapor and carbon dioxide, J. Quant. Spectr. and Radiat. Trans. submitted.

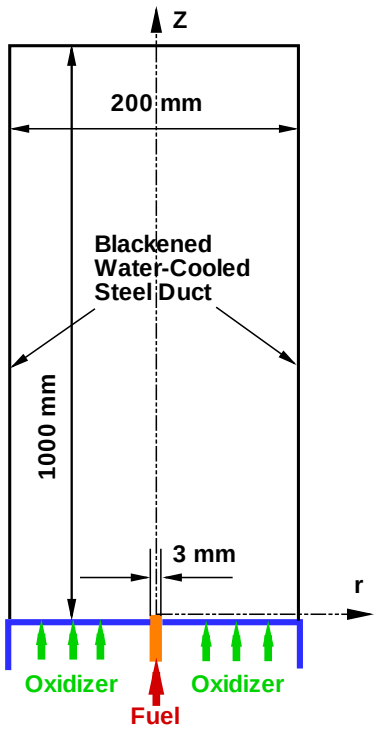

Figure 1. Sketch of burner configuration (not to scale).

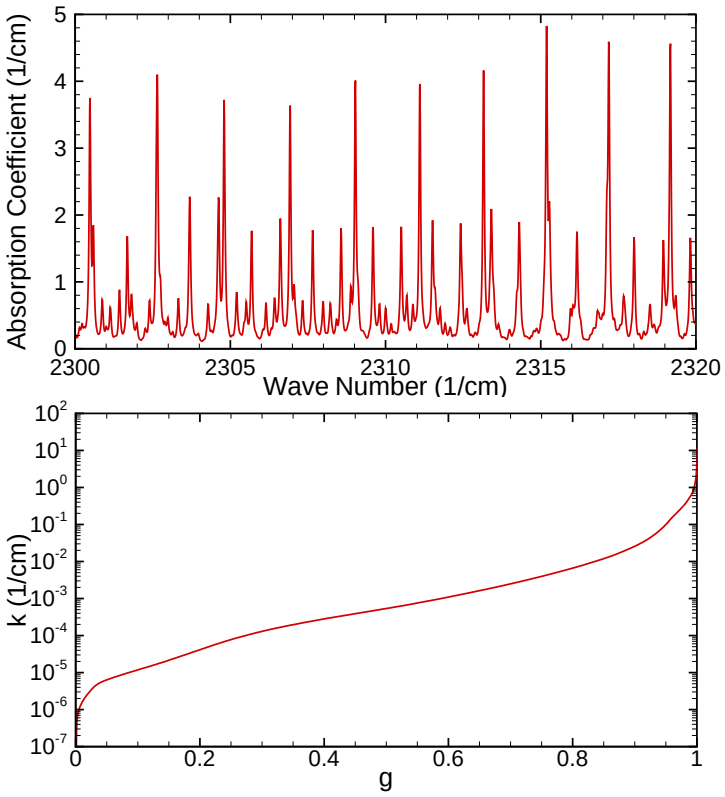

Figure 2. The absorption coefficient (only part of the spectrum is shown) and the corresponding k-g distribution for a 10% CO_2-10% H_2O-80% N_2 mixture at 1000 K and 1 atm.

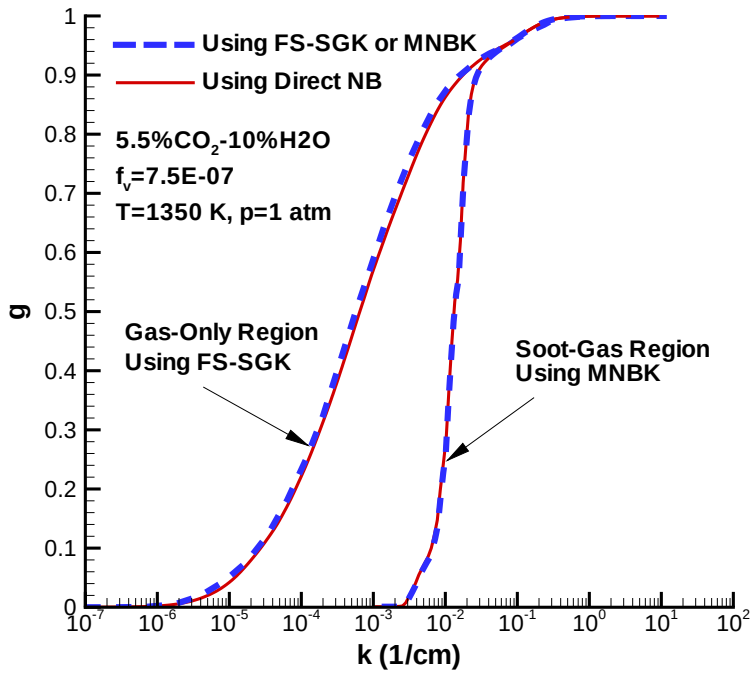

Figure 3. Full-spectrum k vs. g distribution for gas-only and soot-gas region.

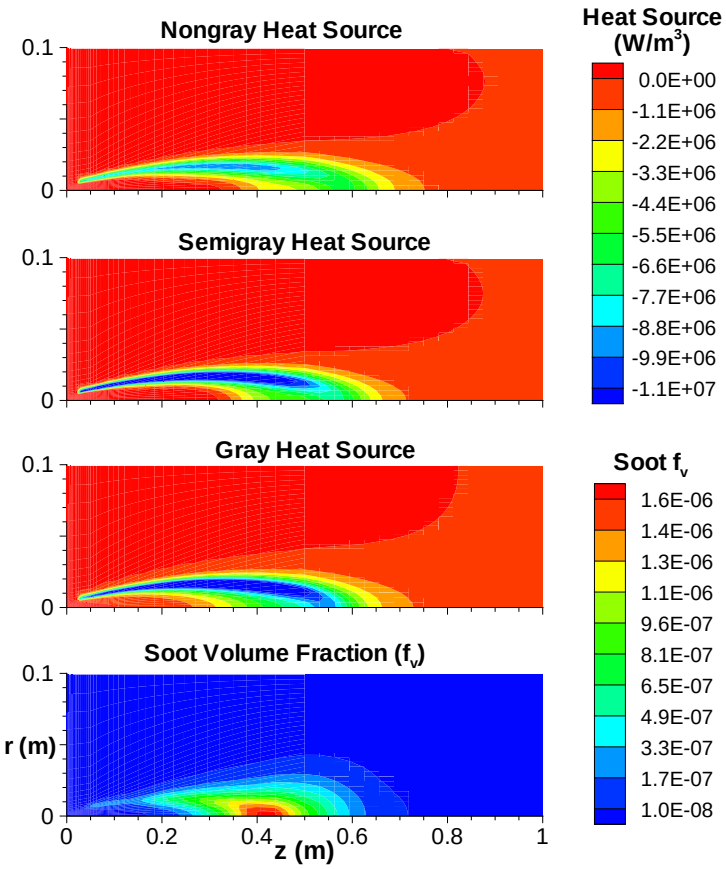

Figure 4. Contours of the computed divergence of radiative heat flux (heat source) and the soot volume fraction (corrected).

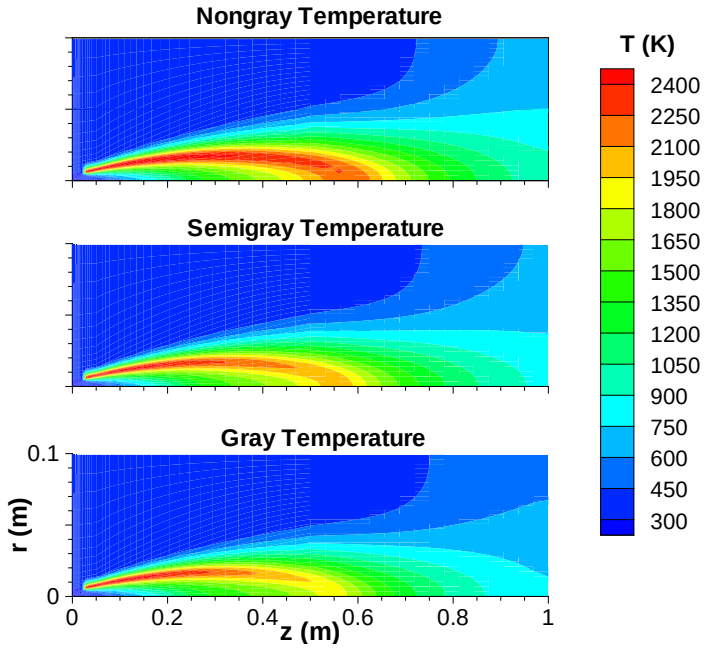

Figure 5. Contours of the computed flame temperature.

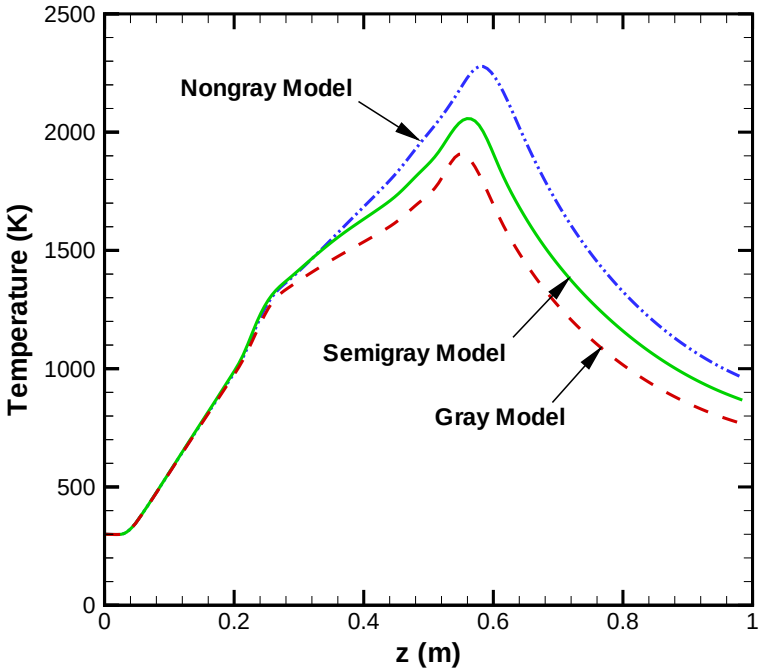

Figure 6. Axial profiles of centerline flame temperature.

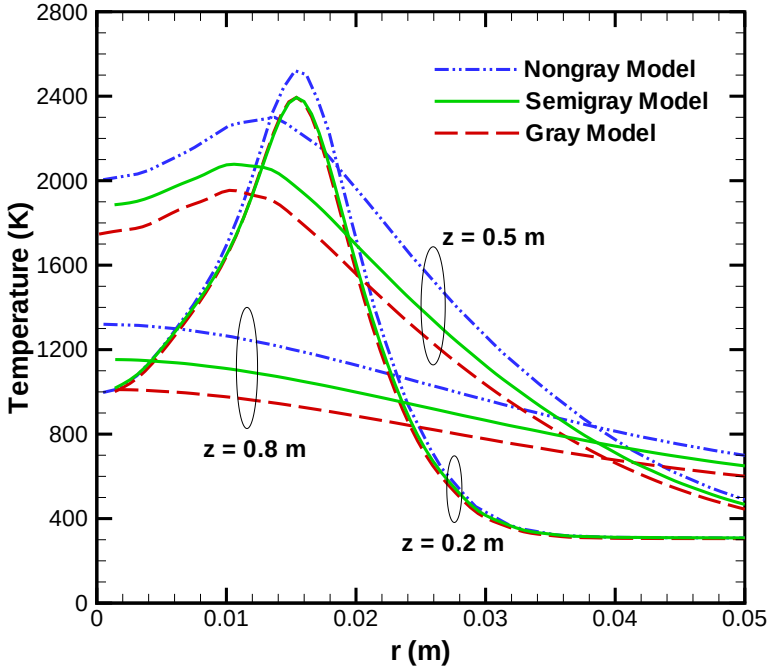

Figure 7. Radial profiles of flame temperature at three axial locations.

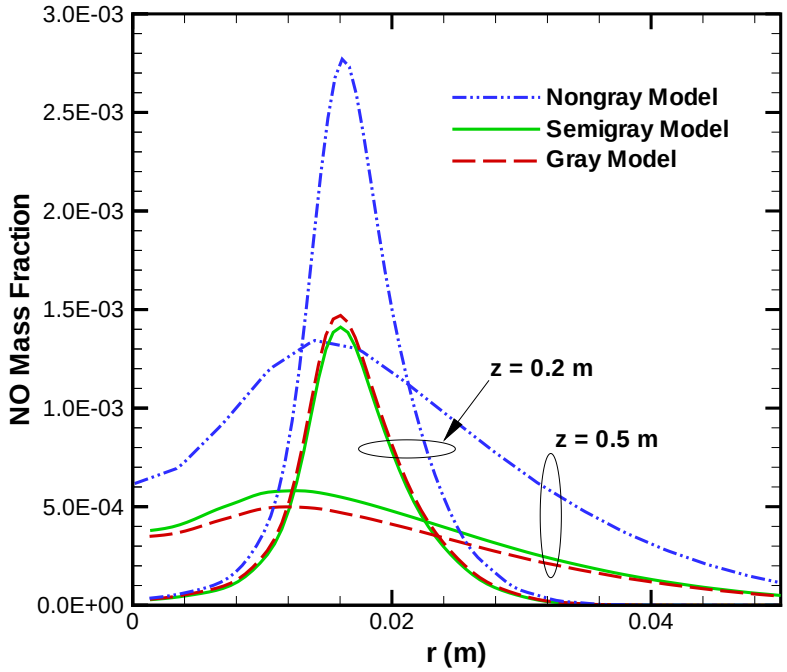

Figure 8. Radial profiles of NO mass fraction at three axial locations.

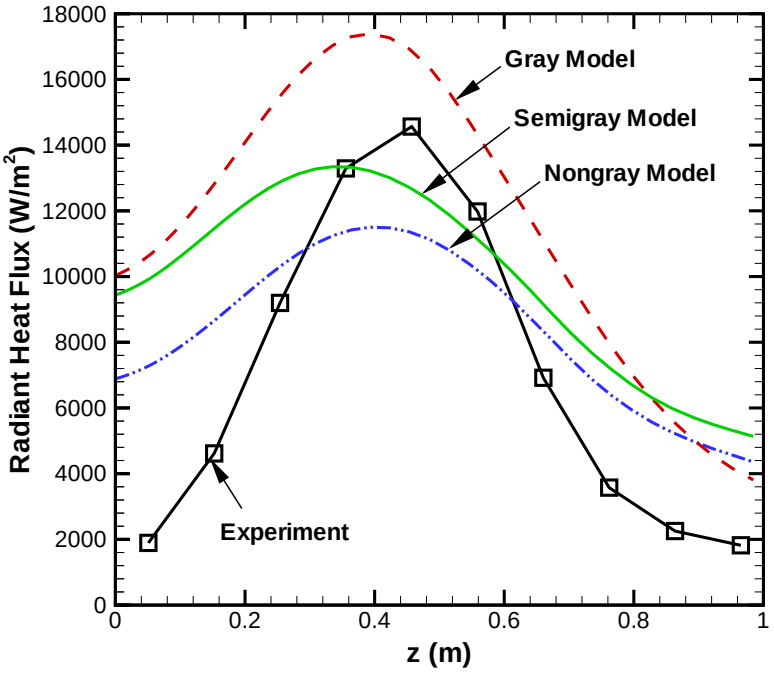

Figure 9. Axial profiles of calculated and measured [26] radiant heat flux at $r = 0.1$ m.

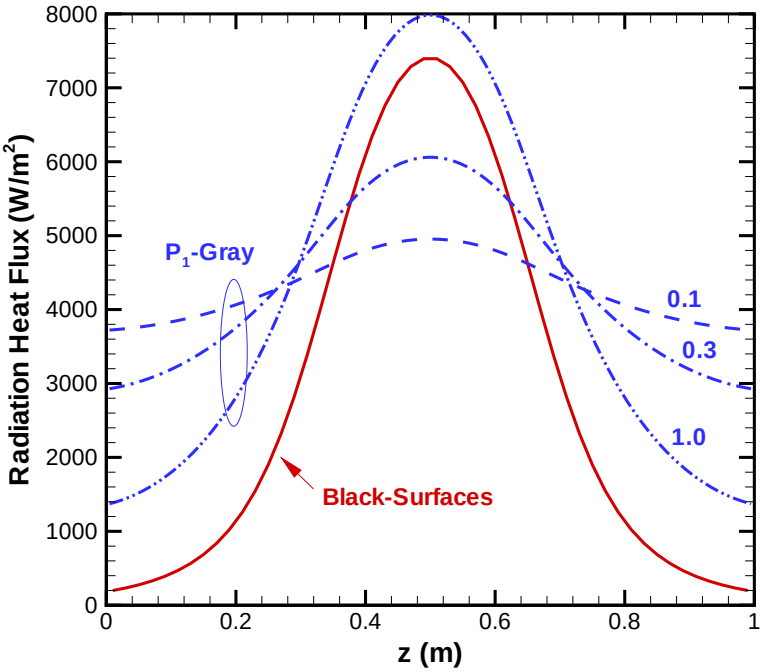

Figure 10. Axial profiles of calculated radiant heat flux to investigate the P_1 approximation.